Hybrid Heterostructures to Generate Long-Lived

and Mobile Photocarriers in Graphene

Pavel Valencia-Acuna,[†] Fatimah Rudayni,^{†,‡} Kushal Rijal,[†] Wai-Lun Chan,^{*,†} and
Hui Zhao^{*,†}

†Department of Physics and Astronomy, The University of Kansas, Lawrence, Kansas 66045, United States

‡Department of Physics, Jazan University, Jazan 45142, Saudi Arabia

E-mail: wlchan@ku.edu; huizhao@ku.edu

Abstract

We report generation of long-lived and highly mobile photocarriers in hybrid van der Waals heterostructures that are formed by monolayer graphene, few-layer transition metal dichalcogenides, and organic semiconductor of F_8ZnPc . Samples are fabricated by dry transfer of mechanically exfoliated MoS_2 or WS_2 few-layer flakes on a graphene film, followed by deposition of F_8ZnPc . Transient absorption microscopy measurements are performed to study the photocarrier dynamics. In heterostructures of F_8ZnPc /few-layer- MoS_2 /graphene, electrons excited in F_8ZnPc can transfer to graphene and thus be separated from the holes that reside in F_8ZnPc . By increasing the thickness of MoS_2 , these electrons acquire long recombination lifetimes of over 100 ps and high mobility of $2800 \text{ cm}^2 \text{ V}^{-1} \text{ s}^{-1}$. Graphene doping with mobile holes is also demonstrated with WS_2 as the middle layers. These artificial heterostructures can improve the performance of graphene-based optoelectronic devices.

Keywords: graphene, van der Waals heterostructure, ultrafast dynamics, diffusion, transient absorption, organic semiconductor

Since its discovery, graphene^{1–4} has been regarded as a promising material for optoelectronic applications due to its superior properties, such as high charge carrier mobilities⁵ and broadband light absorption.⁶ However, the development of graphene-based optoelectronic devices has been hindered by the difficulty of generating free and long-lived photocarriers in graphene with high efficiency. Although light can excite electrons and holes in graphene by interband absorption, they form tightly-bond excitons due to their Coulomb attraction,⁷ which is significantly enhanced in two-dimensional (2D) structures.^{8,9} The formation of the excitons has two consequences that significantly limit the optoelectronic performance of graphene. First, as neutral particles, excitons do not produce a photovoltage due to the lack of charge separation. Second, the exciton recombination lifetime is as short as several picoseconds in graphene, causing rapid loss of absorbed photon energy predominately to the lattice.

Recently, stacking graphene with other 2D materials to form van der Waals heterostructures has shown promise to produce artificial optoelectronic materials. For example, combining graphene with transition metal dichalcogenides (TMDs) was considered beneficial for optoelectronic applications, taking advantage of their superior charge transport and optical absorption properties, respectively. Various devices based on graphene-TMD bilayer heterostructures have been explored, such as photodetectors, 11-13 photovoltaics, 11,14 field-effect transistors, 15-18 memory devices, 19 and vertical tunneling transistors. Whowever, since graphene and TMD form type-I band alignments, both electrons and holes quickly transfer to graphene and recombine. 21-29 Although heterostructures combining graphene with two TMD monolayers 21,30 or two organic semiconductors 31 could separate the carriers and prolong their recombination lifetime, it is unclear whether electrons and holes are still interacting with each other, which limits generation of freely moving charge carriers in graphene.

Here we show that hybrid multilayer van der Waals heterostructures with suitable band alignments can produce long-lived and highly mobile photocarriers in graphene. By combining graphene with few-layer TMDs and organic semiconductor, photoexcited electrons and holes can be spatially separated to different materials to suppress their recombination. With thick TMD middle layers, the electron-hole Coulomb attraction can be reduced, allowing high in-plane mobilities of the charge carriers in graphene. Such artificial materials can enhance the performance of graphene-based optoelectronic devices. Moreover, the strategy demonstrated can be generally applied to design van der Waals heterostructures with finely controlled charge carrier properties at atomic length scales.

Results and Discussion

Heterostructure design and hypothesis on carrier dynamics. The hybrid heterostructures studied are composed of a 2-nm-thick organic semiconductor of fluorinated zinc phthalocyanine (F_8ZnPc), a few-layer (nL) TMD (MoS_2 or WS_2 , $n=1,\ 2,\ 3,\ or\ 4$), and a monolayer graphene (Gr). Figure 1(a) shows the energy band alignment of the heterostructure formed by F₈ZnPc, 1L MoS₂, and graphene. Our ultraviolet photoemission spectroscopy (UPS) measurements (see Methods) show that the lowest unoccupied molecular orbital (LUMO) of F₈ZnPc is about 0.4 eV above the conduction band minimum (CBM) of 1L MoS_2 . With the Dirac point of graphene being below the CBM of MoS_2 , ²² electrons (-) excited in F₈ZnPc experience a laddered band alignment and are expected to transfer to graphene (purple arrow). The same UPS analysis indicates that the highest occupied molecular orbital (HOMO) of F₈ZnPc is about 0.4 eV above the valance band maximum (VBM) of MoS₂. Hence, the photoexcited holes (+) could be confined in F₈ZnPc by the energy barrier of MoS₂. The spatial separation of the electrons and holes is expected to extend their recombination lifetime. For the F₈ZnPc/1L-WS₂/graphene heterostructure, our UPS measurements reveal that the LUMO (HOMO) of F₈ZnPc is lower than the CBM (VBM)

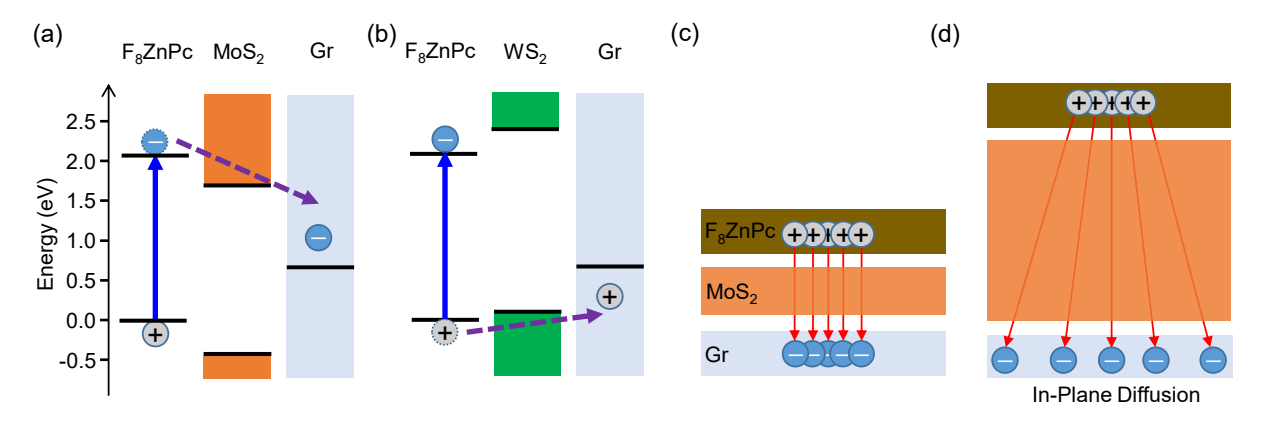


Figure 1: (a) Band alignment of the heterostructure formed by F_8ZnPc , 1L MoS_2 , and graphene. The upper and lower horizontal lines on the left represent the LUMO and HOMO levels of F_8ZnPc . The orange and gray boxes represent the conduction and valence bands of MoS_2 and graphene. Photoexcited electrons (-) are expected to transfer to graphene, while holes (+) reside in F_8ZnPc . (b) Band alignment of the $F_8ZnPc/WS_2/graphene$ heterostructure that allows hole doping of graphene. (c) Schematics of in-plane carrier distributions in $F_8ZnPc/MoS_2/graphene$ in strong binding regime, where the immobile holes in F_8ZnPc prevent free motion of electrons in graphene. (d) Significant in-plane diffusion of electrons in graphene in weak binding regime with thicker MoS_2 middle layer.

of WS₂, allowing holes to transfer to graphene while confining electrons in F₈ZnPc, as illustrated in Figure 1(b). We note that only the carriers excited in F₈ZnPc are shown in Figure 1 for clarity. In experiments with a high photon energy (3.18 eV), all three materials are photoexcited. However, these additional carriers do not change the layer-separated electron-hole population shown in Figure 1 (see detailed discussions in Supporting Information, Figure S1 and S2).

Although the graphene layer can be populated by one type of charge carriers in such heterostructures, their mobility could still be limited. Figure 1(c) shows the situation, using the MoS_2 -based heterostructures as an example, where the electrons in graphene are strongly bound to the holes in F_8ZnPc in forms of interlayer excitons. Hence, the mobility of these electrons is limited by the immobile holes in F_8ZnPc . Our central hypothesis is that, by increasing the thickness of the middle layer, the Coulomb interaction can be reduced by both the dielectric screening effect and the increased charge separation, as schematically illustrated in Figure 1(d), allowing the electrons to move freely in the graphene layer.

Carrier diffusion in $F_8ZnPc/nL-MoS_2/graphene$ heterostructures. The photocarrier dynamics in the $F_8ZnPc/nL-MoS_2/graphene$ heterostructure samples is study by using a homemade transient absorption microscopy setup based on an 80-MHz Ti-doped sapphire laser. ³² For each region of the sample with n=1, 2, 3, or 4, a tightly focused 3.18-eV and 1.4 μ J cm⁻² pump pulse injects photocarriers. By using an absorption coefficient of 10^6 m⁻¹, ³³ the estimated carrier density injected in the F_8ZnPc layer is about 1.1×10^{10} cm⁻². The carriers are detected by measuring differential reflectance of a 1.59-eV probe pulse, $\Delta R/R_0 = (R-R_0)/R_0$, where R and R_0 are the reflectance with and without the pump, respectively. ³² Since the probe photon energy is smaller than the band gaps of MoS₂ and F_8ZnPc , it senses the carriers in graphene, and is proportional to their density. To reveal spatiotemporal dynamics of the carriers, the probe spot is scanned with respect to the pump laser spot, while at each probe position the differential reflectance is measured as a function of the probe delay.

Figure 2(a) - 2(d) shows the measured differential reflectance as a function of the probe delay and probe position for the four regions of n=1,2,3, and 4, respectively. At each probe delay, the spatial profile of the signal reflects the in-plane density distribution of the electrons in graphene. Figure 2(e) - 2(h) each shows several examples of such profiles at various probe delays. If the electrons in graphene are non-interacting and undergo a classical diffusion process, the variance of their spatial distribution evolves as $\sigma^2(t) = \sigma_0^2 + 2Dt$, with D being their diffusion coefficient.³⁴ To compare with this model, the profiles are fit by Gaussian functions, as illustrated by the curves in Figure 2(e) - 2(h). The resulting evolution of the variance is summarized in Figure 2(i) - 2(l) as the black squares. A clear trend of faster electron diffusion with increasing the MoS₂ thickness is observed. With 1L MoS₂, electron diffusion is undetected. This can be attributed to the effect of the holes in F₈ZnPc. Organic semiconductors often possess rather low charge carrier diffusion coefficients. A recent study revealed that in F₈ZnPc, the carrier diffusion coefficient is on the order of 10^{-6} cm² s⁻¹.³⁵ Hence, the hole in-plane distribution largely remains unchanged during the measured

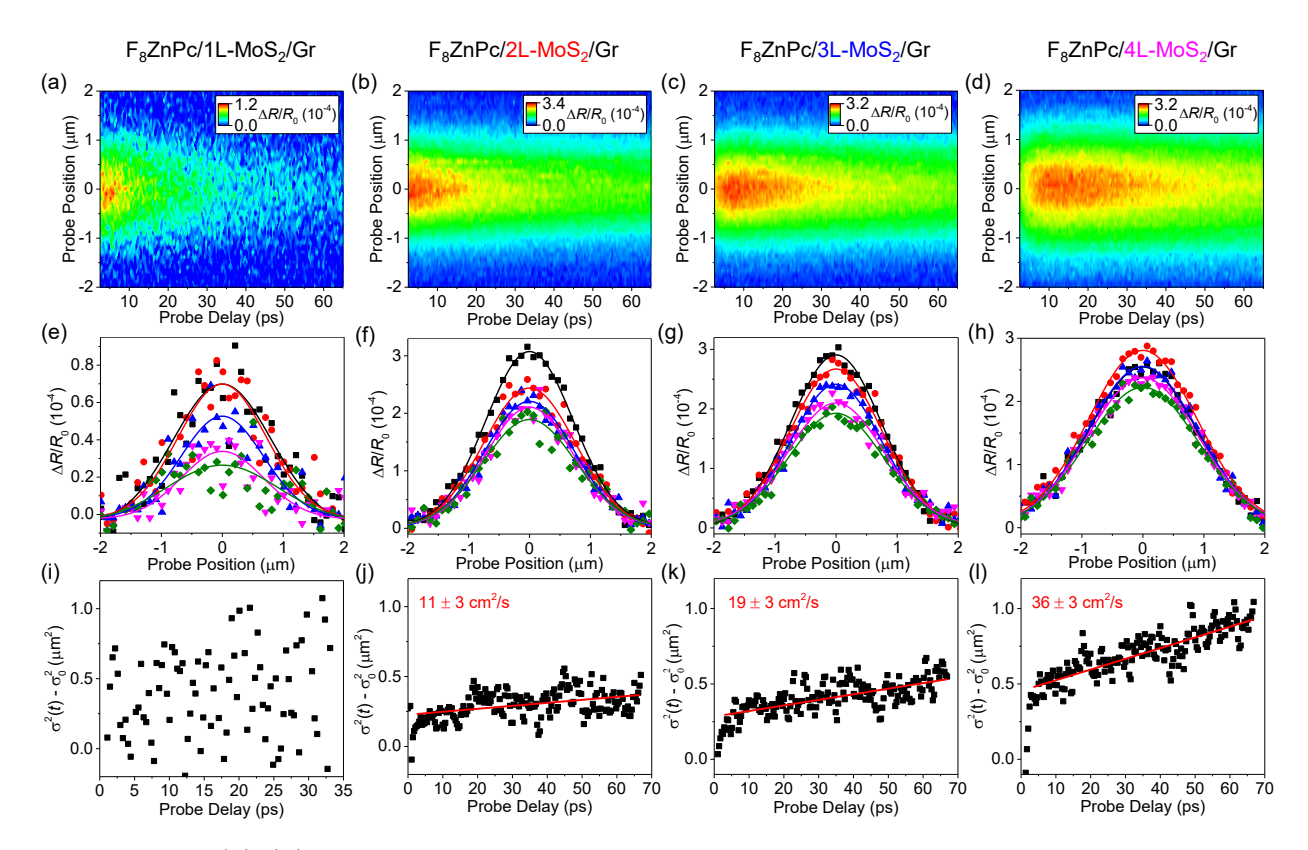


Figure 2: (a)-(d) Spatiotemporally resolved differential reflectance measured from $F_8ZnPc/nL-MoS_2/graphene$ heterostructure samples with n=1, 2, 3, and 4, respectively. (e)-(h) Selected spatial profiles of differential reflectance from the 4 samples. For (e), the probe delays are 2.8 (black), 10.2 (red), 17.7 (blue), 25.1 (pink), and 33.0 ps (green). For (f), (g), and (h), the probe delays are 5.5 (black), 20.4 (red), 35.3 (blue), 50.2 (pink), and 65.0 ps (green). The solid curves are Gaussian fits. (i)-(l) Change of the variance of the spatial distributions as a function of probe delay. Lines are linear fits.

time scale. As schematically illustrated in Figure 1(c), the strong Coulomb attraction from the immobile holes thus prevent diffusion of the electrons. Increasing the MoS₂ thickness, the Coulomb attraction from the holes is reduced due to the larger charge separation and the stronger dielectric screening, resulting in an increase of the diffusion coefficient. With 2L and 3L MoS₂ [Figure 5(j) and 5(k)], the growth of the variance is clearly observed, although the data do not conclusively establish the linear increase. Nevertheless, linear fits to the variance result in diffusion coefficients of 11 and 19 cm² s⁻¹, respectively. For the heterostructures with 4L MoS₂ [Figure 5(l)], the data strongly support a linear expansion, with a diffusion coefficient of 36 cm² s⁻¹. Using Einstein's relation, the diffusion coefficient

of 36 cm² s⁻¹ corresponds to a graphene electron mobility of $\mu = 2eD/k_BT \approx 2800$ cm² V⁻¹ s⁻¹, where e, k_B , and T = 300 K are the elementary charge, the Boltzmann constant, and electron temperature, respectively. The factor of 2 accounts for the linear dispersion of graphene.³⁶ The deduced mobility is comparable to typical values for CVD graphene at room temperature.³⁷ At lower temperatures, the mobility could be enhanced due to the reduced phonon scattering. Even if the electrons are not entirely free from the holes, the significant improvement achieved with 4L MoS₂ is promising for many optoelectronic applications.

Carrier diffusion in $F_8ZnPc/nL-WS_2/graphene$ heterostructures. The hypothesis is further tested with $F_8ZnPc/nL-WS_2/graphene$ heterostructures. As shown in Figure 1(b), here, the holes are expected to transfer to graphene while the electrons will reside in F_8ZnPc . The dynamics of the holes in the graphene layer is studied with the transient absorption microscopy technique under the same conditions. The results are summarized in Figure 3. A trend of faster carrier diffusion in graphene with thicker WS_2 is also observed. However, unlike the MoS_2 -based heterostructures, the expansion of the variance here appears sub-linear. By fitting the data from the heterostructure with 4L WS_2 with an expression of At^p , where A is a constant, we find a power of p = 0.55 [blue curve in Figure 3(i)]. The effective diffusion coefficient (defined according to the derivative of the blue curve) varies from 55 to 13 cm² s⁻¹ [red lines in Figure 3(i)], which are on the same order of magnitude as the results from the heterostructure with 4L MoS_2 . The sub-linear expansion could indicate that the hole diffusion in graphene is still influenced by the electrons in F_8ZnPc . However, more sophisticated modeling is needed to fully understand the difference between the two sets of heterostructures.

To further confirm the trend of the reduction of the Coulomb attraction and the increase of the carrier mobility in graphene with increasing the middle layer thickness, a sample of $F_8ZnPc/7L-WS_2/graphene$ is studied, with results presented in Supporting Information, Figure S5. We obtained a rather linear expansion of the variance, with a diffusion coefficient of 46 ± 3 cm² s⁻¹. However, it should be noted that although a thicker middle layer facilitates

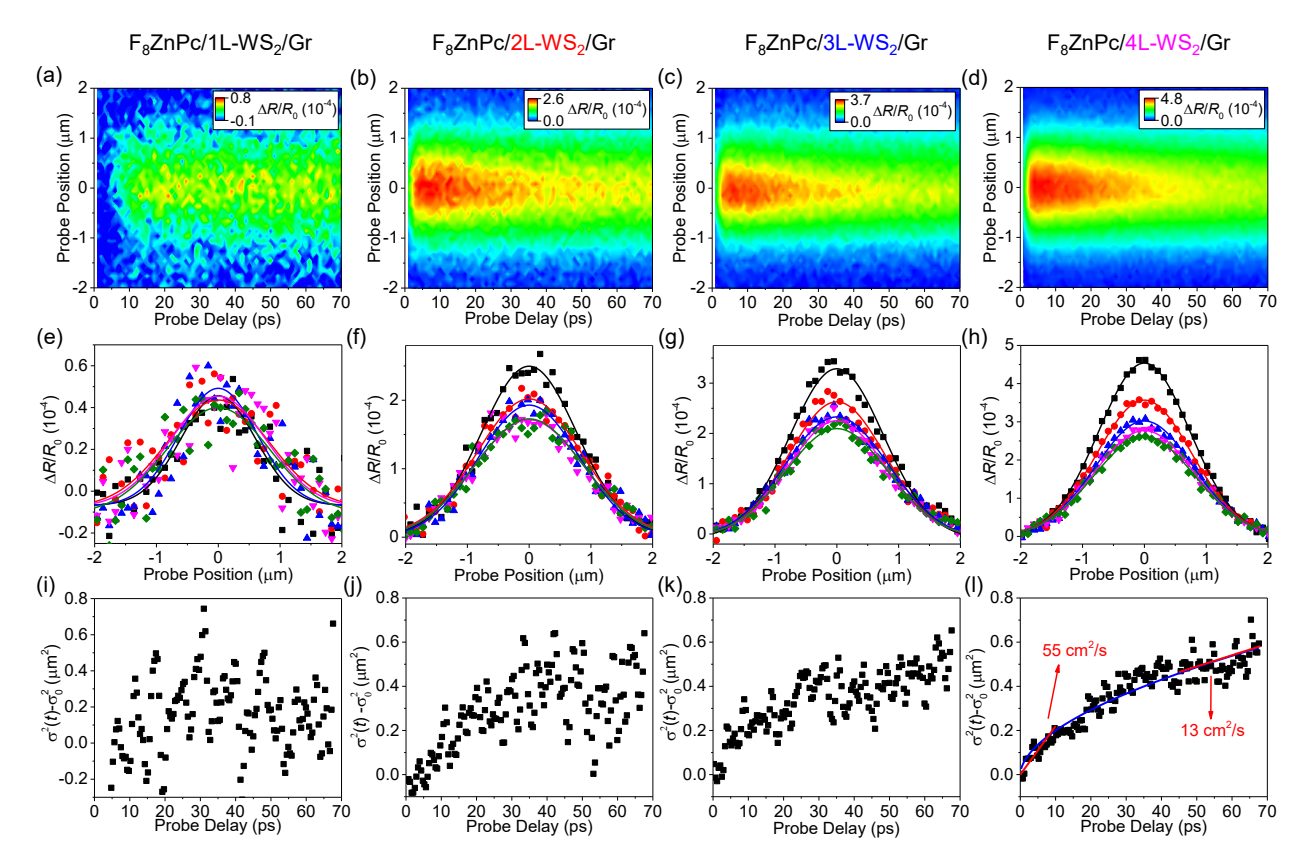


Figure 3: (a)-(d) Spatiotemporally resolved differential reflectance measured from $F_8ZnPc/nL-WS_2/graphene$ heterostructure samples with n=1, 2, 3, and 4, respectively. (e)-(h) Selected spatial profiles of differential reflectance from the 4 samples with probe delays of 5.7 (black), 20.6 (red), 35.5 (blue), 50.4 (pink), and 65.4 ps (green). The solid curves are Gaussian fits. (i)-(l) Change of the variance of the spatial distributions as a function of probe delay. The blue curve in (i) is a fit (see text). Its initial and final slopes (red lines as eye guide) correspond to diffusion coefficients of 55 and 13 cm² s⁻¹, respectively.

free motion of the carriers in graphene, it could compromise interlayer charge transfer and separation efficiency.

Charge-transfer-limited lifetime. We now discuss the decay mechanism of the long-lived signal in both sets of the heterostructures. Figure 4(a) shows the peak signal (that is, at the center of the profile) as a function of the probe delay for the four MoS_2 -based heterostructures. By single-exponential fits (cyan curves), we deduce the decay time constants, as summarized in Figure 4(b). As the number of MoS_2 layer changes from 1 to 4, the decay time constant increases from 25 to 110 ps. All these values are much longer than the electron-hole recombination lifetime of graphene (1.8 \pm 0.2 ps, measured with a monolayer

graphene sample, Figure S3), demonstrating the effect of charge separation. Furthermore, in a control sample of $F_8ZnPc/graphene$ (that is, without the middle TMD layer), the lifetime is as short as 1.6 ± 0.4 ps (Figure S4), since in this case both electrons and holes transfer to graphene. Figure 4(c) illustrates schematically our interpretation of this observation of the thickness-dependent lifetime: Since the electrons and holes are separated to graphene and F_8ZnPc , their recombination requires transfer of the holes from F_8ZnPc to graphene by tunneling through the MoS_2 barrier (purple arrow). With ultrashort recombination lifetime in graphene, the decay time of the signal reflects this tunneling time (or the population lifetime of the holes in F_8ZnPc). Due to the thickness dependent band structure of TMDs, the VBM at Γ point increase with thickness, as indicated by the dashed lines. This lowers the barrier height and thus should enhance the tunneling. However, the barrier width scales linearly with the layer number. Hence, our results show that overall, the tunneling time increases with thickness of MoS_2 . Furthermore, the tunneling-limited lifetime is expected to be insensitive to the lattice temperature.

Interestingly, the decay time shows a different trend in the WS₂-based heterostructures, as summarized in Figure 4(d) and 4(e). The decay in $F_8ZnPc/1L$ -WS₂/graphene is about 250 ps, while with n=2, 3, and 4, the decay times are all about 50 ps. We hypothesize that with n=2, 3, and 4, the CBM of WS₂ drops to below the LUMO level of F_8ZnPc , as indicated in Figure 4(f), allowing band-offset driven electron transfer, instead of tunneling. The decay time of the control sample with 7L WS₂ is about 40 ps [Supporting Information Figure S5(d)], further suggesting that the delay time is independent of thickness for $n \geq 2$. These features suggest the opportunity of designing the type and thickness of the middle layers to engineering the photocarrier lifetime in such hybrid heterostructures. However, more studied, especially computational works, are needed to fully understand some of the observations, such as the rather long lifetime with 1L WS₂ and the opposite trend of the MoS₂-based samples. In both sets of samples, an additional constant component is observed, indicating that there is a long-lived excitation contributing to the signal. We attribute this feature to

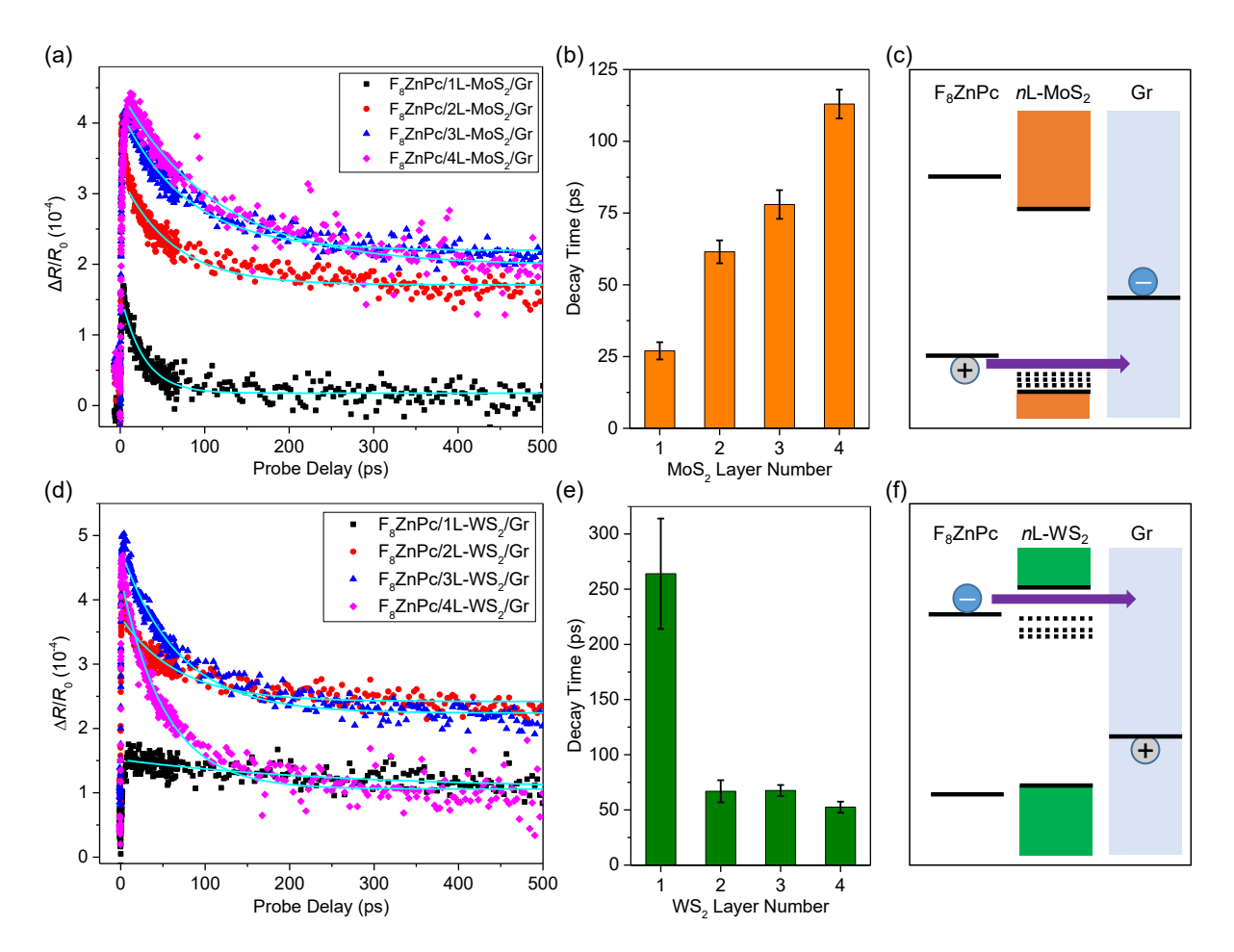


Figure 4: (a) Peak differential reflectance of the MoS_2 -based heterostructure samples as function of probe delay, measured with the pump and probe spots overlapped. The cyan curves are single exponential fits. (b) The deduce decay time constant as a function of the number of layers of MoS_2 . (c) Schematics of the charge recombination model due to the hole tunneling to graphene. (d), (e), and (f) Same as (a), (b), and (c) for the WS_2 -based heterostructure samples.

the charge-transfer excitons formed at F_8ZnPc/TMD interfaces. Such hybrid charge-transfer excitons with long recombination lifetimes can form at organic/inorganic semiconductor interfaces. ^{39–41} In the regions of our samples with poor contact between graphene and TMD layers, charge transfer to graphene can be inefficient, favoring charge-transfer exciton formation.

We emphasize that the trilayer design is a key element to extend the carrier lifetime. Previously, TMD/graphene bilayer heterostructures have been widely studied. ^{10–20} However, since both electrons and holes reside in graphene in such heterostructures, the photocarrier

lifetimes are rather short, in the range of 1 - 4 ps, $^{21-29}$ as summarized in Supporting Information, Table S1. Furthermore, the electron-hole Coulomb interaction and the formation of excitons in graphene could hinder efficient charge separation. The addition of the F₈ZnPc layer in our heterostructures allows only one type of carrier to populate the graphene layer, and with high mobilities.

Recently, many organic semiconductors have been combined with TMDs to form hybrid heterostructures, such as ZnPc, ^{39,42,43} F₈ZnPc, ⁴⁴ H₂Pc, ⁴⁵ CuPc, ⁴⁶ fullerene, ⁴⁷ pentacene, ^{48,49} PTB7, ^{50,51} and P3HT:PCBM. ⁵² In this study, we use F₈ZnPc as the organic layer because its ionization potential can be varied by as much as 1.5 eV by changing the degree of fluorination, ⁵³ which allows us to fine tune the band alignment. In particular, F₈ZnPc forms a type-II band alignment with both MoS₂ and WS₂ while allowing the graphene to be doped with electrons and holes, respectively. However, the demonstrated strategy can be generally applied to other organic semiconductors so long as they form a type-II band alignment with the middle layer.

Conclusions

In summary, we have demonstrated an effective strategy to construct hybrid multilayer heterostructures that can produce long-lived and mobile photocarriers in graphene. By increasing the middle layer thickness of $F_8ZnPc/nL-MoS_2/graphene$ heterostructures, the electrons in graphene can be effectively separated from the holes, resulting in long recombination lifetimes. With reduced Coulomb interaction, the electron mobility of 2800 cm² V⁻¹ s⁻¹ is achieved, as revealed by spatiotemporally resolved transient absorption measurements. Graphene doping with mobile holes is also demonstrated with WS₂ as the middle layers. These artificial heterostructures can improve performance of graphene-based optoelectronic devices.

Methods

Sample fabrication and characterization. To fabricate the F₈ZnPc/nL-MoS₂/graphene heterostructure samples, a thin MoS₂ flake is obtained by mechanical exfoliation from a bulk crystal (acquired from 2D Semiconductors) onto a polydimethylsiloxane (PDMS) substrate. Figure 5(a) shows its microscope image. To identify the thickness of various regions, their green channel contrast is analyzed. The contrast of a certain region of the sample is defined as the difference of the counts of the flake and the substrate, which are proportional to their respective reflectance, normalized by the counts of the substrate. Previous studied have established that the contrast of a thin flake on a thick and transparent substrate is proportional to its thickness.⁵⁴ The inset of Figure 5(b) shows the obtained contrasts for the regions of different thickness, as labeled in (a). The clear step-like feature allows safe assignment of the layer thickness of each region. Furthermore, the contrast of 0.2 is the smallest value obtained after surveying many flakes, further establishing it as the contrast of the smallest possible thickness (1L).

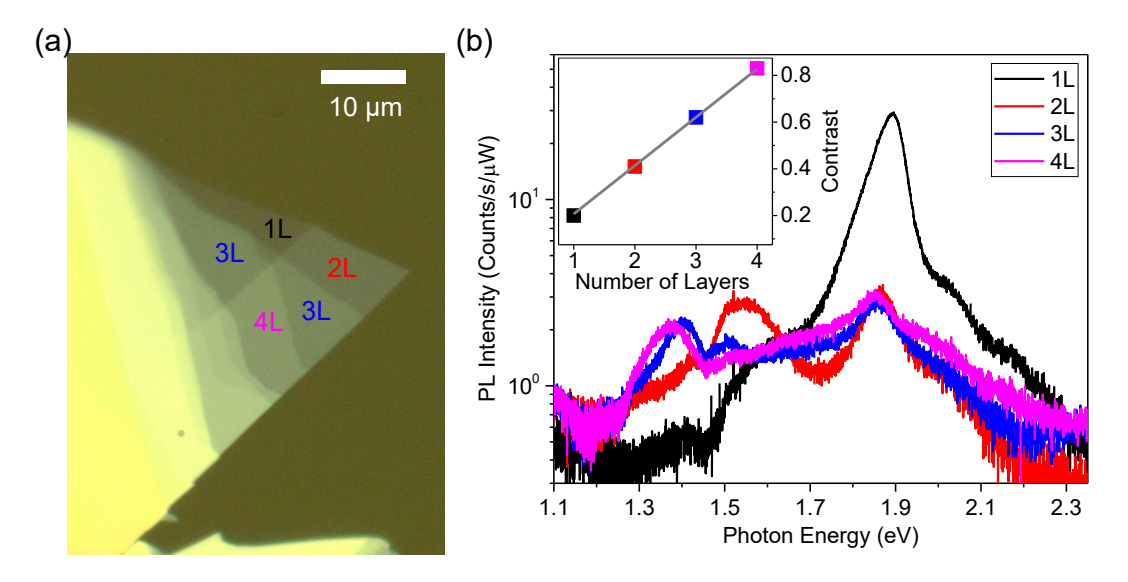


Figure 5: (a) Optical microscope image of the nL-MoS₂ flake. (b) Photoluminescence spectra of different regions of the MoS₂ flake shown in (a). The inset shows the optical contrasts of different regions of the flake.

To further confirm the thickness of the flake and to probe the thickness-dependent

band structures, photoluminescence (PL) spectra from different regions are measured under continuous-wave laser excitation of 3.06 eV and 1 μ W. The laser spot is about 1 μ m in full width at half maximum. The sample is kept in ambient condition at room temperature. The results are shown in Figure 5(b), where the PL intensity is measured by the counts normalized by integration time and excitation power. The peak at about 1.9 eV from the 1L region is consistent with the well-established K valley excitons of 1L MoS₂. ^{55,56} Increasing the thickness, this peak quenches and slightly red shifts, with appearance of a low-energy peak at about 1.55, 1.4, and 1.38 eV for 2L, 3L, and 4L regions, which originate from the indirect transitions between Λ and Γ valleys.

Next, a WS₂ flake is fabricated with the same procedure, as shown in Figure 6. Similar to the MoS₂ flake, the step-like contrast shown in the inset of Figure 6(b) allows assignment of their thickness. PL spectra from this flake are measured under the same conditions as the MoS₂ flake. The bright peak at 2.0 eV from 1L region [black curve in Figure 6(b)] further confirms its thickness, while the indirect peaks at 1.75, 1.60, and 1.50 eV in 2L, 3L, 4L regions, respectively, are in excellent agreement with previously reported PL spectroscopy of few-layer WS₂.⁵⁷

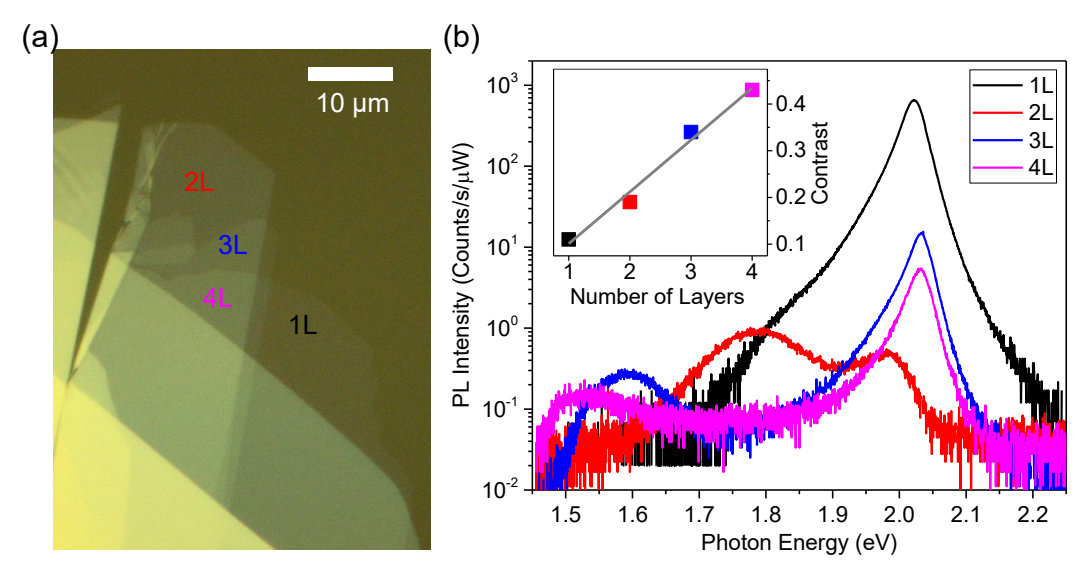


Figure 6: (a) Optical microscope image of the nL-WS₂ flake. (b) Photoluminescence spectra of the different regions of the sample shown in (a). The inset shows the optical contrasts of the different regions of the flake.

To fabricate the heterostructure samples, the MoS_2 and WS_2 flakes are transferred, respectively, to two monolayer graphene films, which are synthesized by chemical vapor deposition (CVD) on quartz substrates (acquired from ACS Materials). Next, a 2-nm layer of F_8ZnPc molecules (99% purity, sublimed, acquired from Luminescence Technology, Taiwan) is deposited on each sample in an ultrahigh vacuum chamber (10^{-9} Torr) at room temperature, with a deposition rate of 0.5 Å/min.

Ultraviolet photoemission spectroscopy. The band alignment of the F_8 ZnPc/TMD interface is determined by using UPS. Because our system does not have μ m-scale spatial resolution, large area and CVD-grown continuous 1Ls of MoS₂ and WS₂ are used. Before the measurement, the MoS₂ and WS₂ films are annealed at 400°C in an ultrahigh vacuum chamber (based pressure: 1×10^{-10} Torr) over night to obtain a clean surface. We collect the photoemitted electrons along the surface normal direction, which corresponds to the Γ point in the k-space. The measured spectra for the MoS_2 and WS_2 films (blue curves) are shown in Figure 7. Unlike bulk crystals, 1L TMD does not has dispersion along the surface normal direction. Therefore, we simply use the peak position as the VBM at the Γ point. We note that the actual VBM for 1L TMD is at the K point. For 1L MoS₂ (WS₂), the VBM at the K point is 0.13-eV^{58} (0.3-eV^{59}) higher than that at the Γ point. These differences are added to the VBM at the Γ point to determine the VBM at the K point. Next, F_8ZnPc films with various thickness are deposited on the TMD. The HOMO peak can be identified in their UPS spectra [Figure 7(a) and 7(b)]. Because F₈ZnPc has a very narrow bandwidth, the peak position is used. The energy offset between the HOMO and the VBM at the K point can be found, which is shown on the energy level diagram on the right of the figure. In the diagram, the HOMO level is set at 0 eV.

To determine the position of the CBM and the LUMO, reported band gaps of these materials are used. We note that these materials have large exciton binding energies. However, we found that the type of band alignment does not change by either using the exciton band gap or the quasiparticle band gap. The exciton band gap can be obtained from the optical

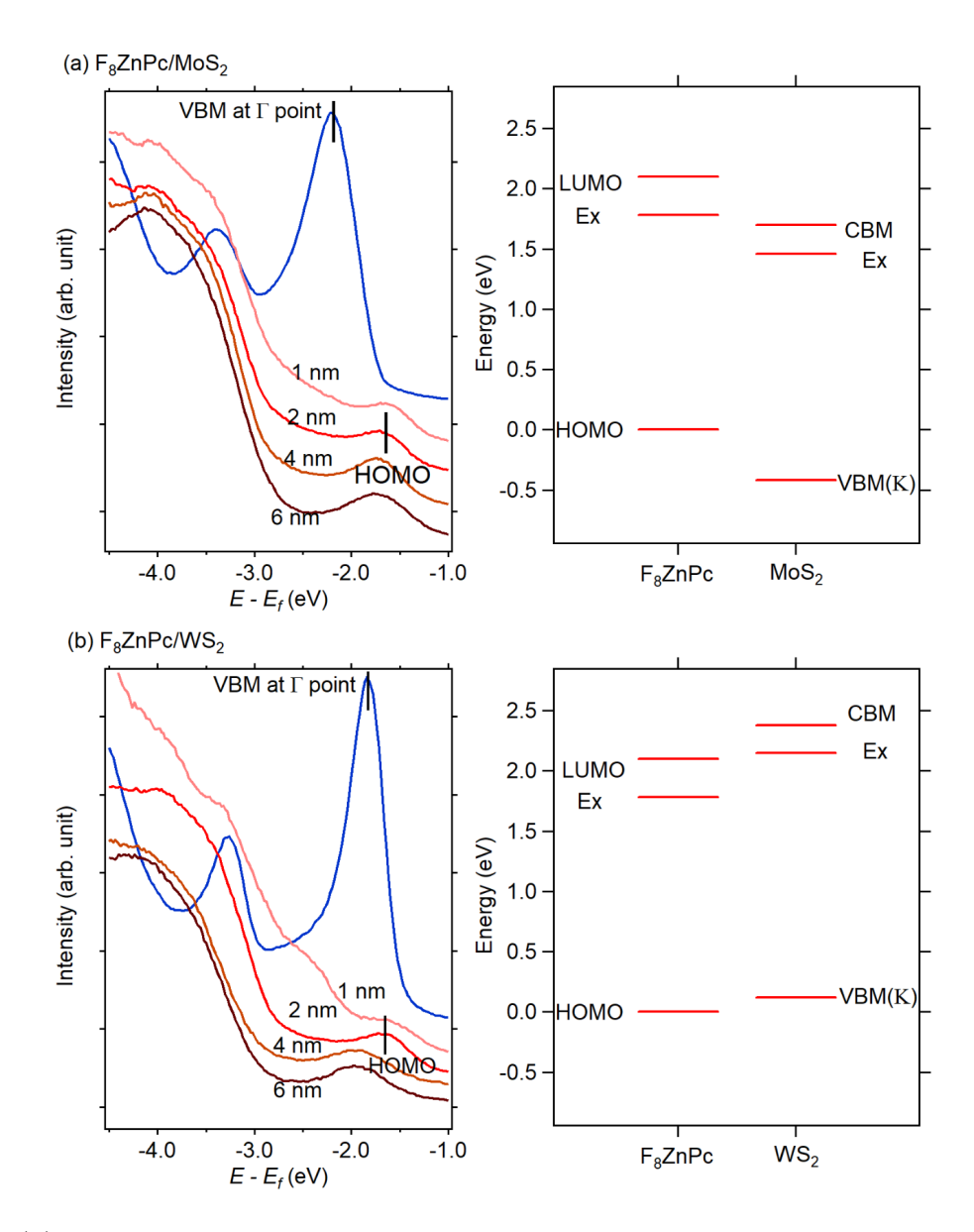


Figure 7: (a) The UPS spectra for CVD-grown 1L MoS_2 and F_8ZnPc films with various thickness deposited on the MoS_2 . The figure on the right shows the energy level diagram derived from the UPS spectra and reported band gaps of these materials. (b) Same as (a), but the MoS_2 is replaced by 1L WS_2 .

absorption spectra (F_8ZnPc : 1.78 eV, 1L MoS₂: 1.88 eV, 1L WS₂: 2.03 eV). These levels are labeled as "Ex" in the band diagram shown in Figure 7. For the quasiparticle band gap, we use an exciton binding energy of 0.24 eV⁶⁰ and 0.23 eV⁶¹ for MoS₂ and WS₂, respectively. We cannot find the quasiparticle band gap for F_8ZnPc in the literature. For similar phthalocyanine molecules, the reported transport gap is in the range of 1.9-2.3 eV.⁶²⁻⁶⁴ Hence, a

value of 2.1 eV is used in the band diagram.

Supporting Information Available

The Supporting Information is available free of charge at https://pubs.acs.org.

Discussion on additional carrier dynamics; Control samples; Heterostructure with a 7L TMD middle layer, summary of previously reported carrier lifetimes in TMD/graphene heterostructures. (PDF).

Notes

The authors declare no competing financial interest.

Acknowledgements

H.Z. acknowledges supported by the U.S. Department of Energy, Office of Basic Energy Sciences, Division of Materials Sciences and Engineering under Award DE-SC0020995. W.-L.C. acknowledges the support by US National Science Foundation grants DMR-2109979. P.V.-A. is supported by KU Research GO and GRF. F.R. acknowledges the scholarship support from Jazan University.

References

- Novoselov, K. S.; Geim, A. K.; Morozov, S. V.; Jiang, D.; Zhang, Y.; Dubonos, S. V.; Grigorieva, I. V.; Firsov, A. A. Electric Field Effect in Atomically Thin Carbon Films. Science 2004, 306, 666–669.
- Novoselov, K. S.; Geim, A. K.; Morozov, S. V.; Jiang, D.; Katsnelson, M. I.; Grigorieva, I. V.; Dubonos, S. V.; Firsov, A. A. Two-Dimensional Gas of Massless Dirac Fermions in Graphene. *Nature* 2005, 438, 197–200.

- 3. Zhang, Y.; Tan, Y. W.; Stormer, H. L.; Kim, P. Experimental observation of the quantum Hall effect and Berry's phase in graphene. *Nature* **2005**, *438*, 201–204.
- Kim, K. S.; Zhao, Y.; Jang, H.; Lee, S. Y.; Kim, J. M.; Kim, K. S.; Ahn, J. H.; Kim, P.;
 Choi, J. Y.; Hong, B. H. Large-Scale Pattern Growth of Graphene Films for Stretchable
 Transparent Electrodes. *Nature* 2009, 457, 706.
- 5. Geim, A. K.; Novoselov, K. S. The Rise of Graphene. *Nat. Mater.* **2007**, *6*, 183–191.
- Nair, R. R.; Blake, P.; Grigorenko, A. N.; Novoselov, K. S.; Booth, T. J.; Stauber, T.;
 Peres, N. M. R.; Geim, A. K. Fine structure constant defines visual transparency of graphene. Science 2008, 320, 1308.
- Yang, L.; Deslippe, J.; Park, C.-H.; Cohen, M. L.; Louie, S. G. Excitonic Effects on the Optical Response of Graphene and Bilayer Graphene. *Phys. Rev. Lett.* 2009, 103, 186802.
- 8. He, K.; Kumar, N.; Zhao, L.; Wang, Z.; Mak, K. F.; Zhao, H.; Shan, J. Tightly Bound Excitons in Monolayer WSe₂. *Phys. Rev. Lett.* **2014**, *113*, 026803.
- Chernikov, A.; Berkelbach, T. C.; Hill, H. M.; Rigosi, A.; Li, Y. L.; Aslan, O. B.; Reichman, D. R.; Hybertsen, M. S.; Heinz, T. F. Exciton Binding Energy and Nonhydrogenic Rydberg Series in Monolayer WS₂. Phys. Rev. Lett. 2014, 113, 076802.
- Shi, J. P.; Liu, M. X.; Wen, J. X.; Ren, X. B.; Zhou, X. B.; Ji, Q. Q.; Ma, D. L.; Zhang, Y.;
 Jin, C. H.; Chen, H. J.; Deng, S. Z.; Xu, N. S.; Liu, Z. F.; Zhang, Y. F. All Chemical Vapor Deposition Synthesis and Intrinsic Bandgap Observation of MoS₂/Graphene Heterostructures. Adv. Mater. 2015, 27, 7086.
- Yu, W. J.; Liu, Y.; Zhou, H.; Yin, A.; Li, Z.; Huang, Y.; Duan, X. Highly Efficient Gate-Tunable Photocurrent Generation in Vertical Heterostructures of Layered Materials. *Nat. Nanotechnol.* 2013, 8, 952–958.

- 12. Fazio, D. D.; Goykhman, I.; Yoon, D.; Bruna, M.; Eiden, A.; Milana, S.; Sassi, U.; Barbone, M.; Dumcenco, D.; Marinov, K.; Kis, A.; Ferrari, A. C. High Responsivity, Large-Area Graphene/MoS₂ Flexible Photodetectors. *ACS Nano* **2016**, *10*, 8252–8262.
- 13. Yu, W. J.; Vu, Q. A.; Oh, H.; Nam, H. G.; Zhou, H. L.; Cha, S.; Kim, J. Y.; Carvalho, A.; Jeong, M.; Choi, H.; Neto, A. H. C.; Lee, Y. H.; Duan, X. F. Unusually Efficient Photocurrent Extraction in Monolayer van der Waals Heterostructure by Tunnelling through Discretized Barriers. Nat. Commun. 2016, 7, 13278.
- 14. Britnell, L.; Ribeiro, R. M.; Eckmann, A.; Jalil, R.; Belle, B. D.; Mishchenko, A.; Kim, Y.-J.; Gorbachev, R. V.; Georgiou, T.; Morozov, S. V.; Grigorenko, A. N.; Geim, A. K.; Casiraghi, C.; Neto, A. H. C.; Novoselov, K. S. Strong Light-Matter Interactions in Heterostructures of Atomically Thin Films. Science 2013, 340, 1311–1314.
- Yu, W. J.; Li, Z.; Zhou, H. L.; Chen, Y.; Wang, Y.; Huang, Y.; Duan, X. F. Vertically Stacked Multi-Heterostructures of Layered Materials for Logic Transistors and Complementary Inverters. *Nat. Mater.* 2013, 12, 246–252.
- Britnell, L.; Gorbachev, R. V.; Jalil, R.; Belle, B. D.; Schedin, F.; Mishchenko, A.;
 Georgiou, T.; Katsnelson, M. I.; Eaves, L.; Morozov, S. V.; Peres, N. M. R.; Leist, J.;
 Geim, A. K.; Novoselov, K. S.; Ponomarenko, L. A. Field-Effect Tunneling Transistor
 Based on Vertical Graphene Heterostructures. Science 2012, 335, 947–950.
- 17. Shih, C. J.; Wang, Q. H.; Son, Y.; Jin, Z.; Blankschtein, D.; Strano, M. S. Tuning On-Off Current Ratio and Field-Effect Mobility in a MoS₂-Graphene Heterostructure via Schottky Barrier Modulation. ACS Nano 2014, 8, 5790–5798.
- Kwak, J. Y.; Hwang, J.; Calderon, B.; Alsalman, H.; Munoz, N.; Schutter, B.; Spencer, M. G. Electrical Characteristics of Multilayer MoS₂ FET's with MoS₂/Graphene Heterojunction Contacts. *Nano Lett.* 2014, 14, 4511–4516.

- Roy, K.; Padmanabhan, M.; Goswami, S.; Sai, T. P.; Ramalingam, G.; Raghavan, S.;
 Ghosh, A. Graphene-MoS₂ Hybrid Structures for Multifunctional Photoresponsive Memory Devices. *Nat. Nanotechnol.* 2013, 8, 826–830.
- 20. Sata, Y.; Moriya, R.; Morikawa, S.; Yabuki, N.; Masubuchi, S.; Machida, T. Electric Field Modulation of Schottky Barrier Height in Graphene/MoS₂ van der Waals Heterointerface. *Appl. Phys. Lett.* **2015**, *107*, 023109.
- 21. Lane, S. D.; Zhao, H. Unipolar Optical Doping and Extended Photocarrier Lifetime in Graphene by Band-Alignment Engineering. *Nano Futures* **2018**, *2*, 035003.
- 22. Tran, M. D.; Lee, S.-G.; Jeon, S.; Kim, S.-T.; Kim, H.; Nguyen, V. L.; Adhikari, S.; Woo, S.; Park, H. C.; Kim, Y.; Kim, J.-H.; Lee, Y. H. Decelerated Hot Carrier Cooling in Graphene Via Nondissipative Carrier Injection from MoS₂. ACS Nano 2020, 14, 13905–13912.
- 23. Luo, D.; Tang, J.; Shen, X.; Ji, F.; Yang, J.; Weathersby, S.; Kozina, M. E.; Chen, Z.; Xiao, J.; Ye, Y.; Cao, T.; Zhang, G.; Wang, X.; Lindenberg, A. M. Twist-Angle-Dependent Ultrafast Charge Transfer in Mos₂-Graphene van der Waals Heterostructures. Nano Lett. 2021, 21, 8051–8057.
- 24. He, J.; Kumar, N.; Bellus, M. Z.; Chiu, H. Y.; He, D.; Wang, Y.; Zhao, H. Electron Transfer and Coupling in Graphene-Tungsten Disulfide van der Waals Heterostructures. Nat. Commun. 2014, 5, 5622.
- Yuan, L.; Chung, T. F.; Kuc, A.; Wan, Y.; Xu, Y.; Chen, Y. P.; Heine, T.; Huang, L. B. Photocarrier Generation from Interlayer Charge-Transfer Transitions in WS₂-Graphene Heterostructures. Sci. Adv. 2018, 4, e1700324.
- 26. Aeschlimann, S.; Rossi, A.; Chavez-Cervantes, M.; Krause, R.; Arnoldi, B.; Stadtmuller, B.; Aeschlimann, M.; Forti, S.; Fabbri, F.; Coletti, C.; Gierz, I. Direct Evidence

- for Efficient Ultrafast Charge Separation in Epitaxial WS_2 /Graphene Heterostructures. Sci. Adv. **2020**, 6, eaay0761.
- 27. Ferrante, C.; Battista, G. D.; Lopez, L. E. P.; Batignani, G.; Lorchat, E.; Virga, A.; Berciaud, S.; Scopigno, T. Picosecond Energy Transfer in a Transition Metal Dichalcogenide-Graphene Heterostructure Revealed by Transient Raman Spectroscopy. Proc. Natl. Acad. Sci. U.S.A. 2022, 119, e2119726119.
- 28. Tan, Y.; Liu, X. B.; He, Z. L.; Liu, Y. R.; Zhao, M. W.; Zhang, H.; Chen, F. Tuning of Interlayer Coupling in Large-Area Graphene/WSe₂ van der Waals Heterostructure Via Ion Irradiation: Optical Evidences and Photonic Applications. ACS Photo. 2017, 4, 1531–1538.
- Zhou, H. Z.; Chen, Y. Z.; Zhu, H. M. Deciphering Asymmetric Charge Transfer at Transition Metal Dichalcogenide-Graphene Interface by Helicity-Resolved Ultrafast Spectroscopy. Sci. Adv. 2021, 7, eabg2999.
- 30. Chen, Y.; Sun, C.; Zhou, H.; Li, J.; Xin, W.; Xu, H.; Zhu, H. Controlling Photocarrier Lifetime in Graphene for Enhanced Photocurrent Generation via Cascade Hot Electron Transfer. J. Phys. Chem. Lett. 2021, 12, 9989–9994.
- 31. Kattel, B.; Qin, L.; Kafle, T. R.; Chan, W. L. Graphene Field-Effect Transistor as a High-Throughput Platform to Probe Charge Separation at Donor-Acceptor Interfaces.

 J. Phys. Chem. Lett. 2018, 9, 1633–1641.
- 32. Ceballos, F.; Zhao, H. Ultrafast Laser Spectroscopy of Two-Dimensional Materials beyond Graphene. *Adv. Funct. Mater.* **2017**, *27*, 1604509.
- 33. Brendel, M.; Krause, S.; Steindamm, A.; Topczak, A. K.; Sundarraj, S.; Erk, P.; Höhla, S.; Fruehauf, N.; Koch, N.; Pflaum, J. The Effect of Gradual Fluorination on the Properties of F_nZnPc Thin Films and F_nZnPc/C₆₀ Bilayer Photovoltaic Cells. Adv. Funct. Mater. **2015**, 25, 1565–1573.

- 34. Ginsberg, N. S.; Tisdale, W. A. Spatially Resolved Photogenerated Exciton and Charge Transport in Emerging Semiconductors. *Annu. Rev. Phys. Chem.* **2020**, *71*, 1–30.
- 35. Warren, P. R.; Hardigree, J. F. M.; Lauritzen, A. E.; Nelson, J.; Riede, M. Tuning the ambipolar behaviour of organic field effect transistors *via* band engineering. *AIP Adv.* **2019**, *9*, 035202.
- 36. Rengel, R.; Martín, M. J. Diffusion coefficient, correlation function, and power spectral density of velocity fluctuations in monolayer graphene. *J. Appl. Phys.* **2013**, *114*, 143702.
- 37. Fazio, D. D.; Purdie, D. G.; Ott, A. K.; Braeuninger-Weimer, P.; Khodkov, T.; Goossens, S.; Taniguchi, T.; Watanabe, K.; Livreri, P.; Koppens, F. H. L.; Hofmann, S.; Goykhman, I.; Ferrari, A. C.; Lombardo, A. High-Mobility, Wet-Transferred Graphene Grown by Chemical Vapor Deposition. ACS Nano 2019, 13, 8926–8935.
- 38. Kim, H.; Choi, H. J. Thickness Dependence of Work Function, Ionization Energy, and Electron Affinity of Mo and W Dichalcogenides from DFT and GW Calculations. *Phy. Rev. B* **2021**, *103*, 085404.
- 39. Kafle, T.; Kattel, B.; Lane, S. D.; Wang, T.; Zhao, H.; Chan, W. L. Charge Transfer Exciton and Spin Flipping at Organic-Transition Metal Dichalcogenide Interfaces. ACS Nano 2017, 11, 10184–10192.
- 40. Markeev, P. A.; Najafidehaghani, E.; Samu, G. F.; Sarosi, K.; Kalkan, S. B.; Gan, Z.; George, A.; Reisner, V.; Mogyorosi, K.; Chikan, V.; Nickel, B.; Turchanin, A.; de Jong, M. P. Exciton Dynamics in MoS₂-Pentacene and WSe₂-Pentacene Heterojunctions. ACS Nano 2022, 16, 16668–16676.
- 41. Ye, L.; Xu, X.; He, S.; Liu, Y.; Jin, Y.; Yang, Y. M.; Zhu, H. Molecular Triplet Sensitization of Monolayer Semiconductors in 2D Organic/Inorganic Hybrid Heterostructures.

 ACS Nano 2022, 16, 12532–12540.

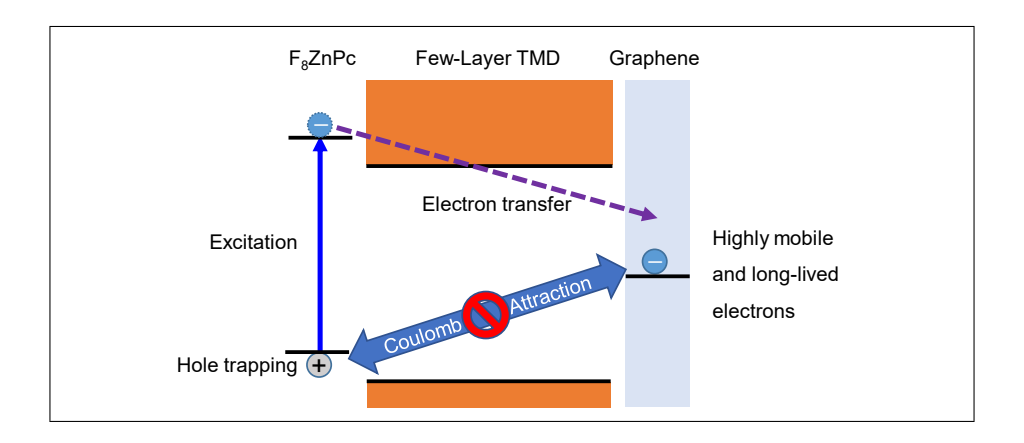
- 42. Kafle, T. R.; Kattel, B.; Yao, P.; Zereshki, P.; Zhao, H.; Chan, W. L. Effect of the Interfacial Energy Landscape on Photoinduced Charge Generation at the ZnPc/MoS₂ Interface. J. Am. Chem. Soc. **2019**, 141, 11328–11336.
- 43. Canton-Vitoria, R.; Gobeze, H. B.; Blas-Ferrando, V. M.; Ortiz, J.; Jang, Y.; Fernandez-Lazaro, F.; Sastre-Santos, A.; Nakanishi, Y.; Shinohara, H.; D'Souza, F.; Tagmatarchis, N. Excited-State Charge Transfer in Covalently Functionalized MoS₂ with a Zinc Phthalocyanine Donor-Acceptor Hybrid. Angew. Chem.-Int. Edit. 2019, 58, 5712–5717.
- 44. Valencia-Acuna, P.; Kafle, T. R.; Zereshki, P.; Peelaers, H.; Chan, W. L.; Zhao, H. Ultrafast Hole Transfer from Monolayer ReS₂ to Thin-Film F₈ZnPc. *Appl. Phys. Lett.* **2021**, *118*, 153104.
- 45. Mutz, N.; Park, S.; Schultz, T.; Sadofev, S.; Dalgleish, S.; Reissig, L.; Koch, N.; List-Kratochvil, E. J. W.; Blumstengel, S. Excited-State Charge Transfer Enabling MoS₂/Phthalocyanine Photodetectors with Extended Spectral Sensitivity. J. Phys. Chem. C 2020, 124, 2837–2843.
- 46. Amsterdam, S. H.; Stanev, T. K.; Zhou, Q.; Lou, A. J. T.; Bergeron, H.; Darancet, P.; Hersam, M. C.; Stern, N. P.; Marks, T. J. Electronic Coupling in Metallophthalocyanine—Transition Metal Dichalcogenide Mixed-Dimensional Heterojunctions. ACS Nano 2019, 13, 4183–4190.
- 47. Rijal, K.; Rudayni, F.; Kafle, T. R.; Chan, W.-L. Collective Effects of Band Offset and Wave Function Dimensionality on Impeding Electron Transfer from 2D to Organic Crystals. J. Phys. Chem. Lett. 2020, 11, 7495–7501.
- 48. Jariwala, D.; Howell, S. L.; Chen, K. S.; Kang, J. M.; Sangwan, V. K.; Filippone, S. A.; Turrisi, R.; Marks, T. J.; Lauhon, L. J.; Hersam, M. C. Hybrid, Gate-Tunable, van der Waals p-n Heterojunctions from Pentacene and MoS₂. Nano Lett. **2016**, 16, 497–503.

- 49. Homan, S. B.; Sangwan, V. K.; Balla, I.; Bergeron, H.; Weiss, E. A.; Hersam, M. C. Ultrafast Exciton Dissociation and Long-Lived Charge Separation in a Photovoltaic Pentacene-MoS₂ van der Waals Heterojunction. *Nano Lett.* **2017**, *17*, 164–169.
- 50. Zhong, C. M.; Sangwan, V. K.; Wang, C.; Bergeron, H.; Hersam, M. C.; Weiss, E. A. Mechanisms of Ultrafast Charge Separation in a PTB7/Monolayer MoS₂ van der Waals Heterojunction. J. Phys. Chem. Lett. 2018, 9, 2484–2491.
- 51. Liu, X.-Y.; Chen, W.-K.; Fang, W.-H.; Cui, G. Nonadiabatic Dynamics Simulations Reveal Distinct Effects of the Thickness of PTB7 on Interfacial Electron and Hole Transfer Dynamics in PTB7@MoS₂ Heterostructures. J. Phys. Chem. Lett. 2019, 10, 2949–2956.
- 52. Petoukhoff, C. E.; Krishna, M. B. M.; Voiry, D.; Bozkurt, I.; Deckoff-Jones, S.; Chhowalla, M.; O'Carroll, D. M.; Dani, K. M. Ultrafast Charge Transfer and Enhanced Absorption in MoS₂-Organic van der Waals Heterojunctions Using Plasmonic Metasurfaces. ACS Nano 2016, 10, 9899–9908.
- 53. Schwarze, M.; Tress, W.; Beyer, B.; Gao, F.; Scholz, R.; Poelking, C.; Ortstein, K.; Günther, A. A.; Kasemann, D.; Andrienko, D.; Leo, K. Band Structure Engineering in Organic Semiconductors. *Science* **2016**, *352*, 1446–1449.
- 54. Cui, Q.; He, J.; Bellus, M. Z.; Mirzokarimov, M.; Hofmann, T.; Chiu, H.-Y.; Antonik, M.; He, D.; Wang, Y.; Zhao, H. Transient Absorption Measurements on Anisotropic Monolayer ReS₂. Small **2015**, 11, 5565–5571.
- 55. Mak, K. F.; Lee, C.; Hone, J.; Shan, J.; Heinz, T. F. Atomically Thin MoS₂: A New Direct-Gap Semiconductor. *Phys. Rev. Lett.* **2010**, *105*, 136805.
- 56. Splendiani, A.; Sun, L.; Zhang, Y.; Li, T.; Kim, J.; Chim, C. Y.; Galli, G.; Wang, F. Emerging Photoluminescence in Monolayer MoS₂. Nano Lett. **2010**, 10, 1271–1275.

- 57. Zeng, H.; Liu, G.-B.; Dai, J.; Yan, Y.; Zhu, B.; He, R.; Xie, L.; Xu, S.; Chen, X.; Yao, W.; Cui, X. Optical Signature of Symmetry Variations and Spin-Valley Coupling in Atomically Thin Tungsten Dichalcogenides. *Sci. Rep.* **2013**, *3*, 1608.
- 58. Jin, W.; Yeh, P.-C.; Zaki, N.; Zhang, D.; Sadowski, J. T.; Al-Mahboob, A.; van der Zande, A. M.; Chenet, D. A.; Dadap, J. I.; Herman, I. P.; Sutter, P.; Hone, J.; R. M. Osgood, J. Direct measurement of the thickness-dependent electronic band structure of MoS₂ using angle-resolved photoemission spectroscopy. *Phys. Rev. Lett.* 2013, 111, 106801.
- 59. Henck, H.; Aziza, Z. B.; Pierucci, D.; Laourine, F.; Reale, F.; Palczynski, P.; Chaste, J.; Silly, M. G.; Bertran, F.; Fèvre, P. L.; Lhuillier, E.; Wakamura, T.; Mattevi, C.; Rault, J. E.; Calandra, M.; Ouerghi, A. Electronic Band Structure of Two-Dimensional WS₂/Graphene van Der Waals Heterostructures. *Phy. Rev. B* 2018, *97*, 155421.
- 60. Park, S.; Mutz, N.; Schultz, T.; Blumstengel, S.; Han, A.; Aljarb, A.; Li, L. J.; List-Kratochvil, E. J. W.; Amsalem, P.; Koch, N. Direct Determination of Monolayer MoS₂ and WSe₂ Exciton Binding Energies on Insulating and Metallic Substrates. 2D Mater. 2018, 5, 025003.
- 61. Hsu, W.-T.; Quan, J.; Wang, C.-Y.; Lu, L.-S.; Campbell, M.; Chang, W.-H.; Li, L.-J.; Li, X.; Shih, C.-K. Dielectric Impact on Exciton Binding Energy and Quasiparticle Bandgap in Monolayer WS₂ and WSe₂. 2D Mater. 2019, 6, 025028.
- 62. Gao, W.; Kahn, A. Electronic Structure and Current Injection in Zinc Phthalocyanine Doped with Tetrafluorotetracyanoquinodimethane: Interface Versus Bulk Effects. Org. Electron. 2002, 3, 53–63.
- 63. Zahn, D. R. T.; Gavrila, G. N.; Gorgoi, M. The Transport Gap of Organic Semiconductors Studied Using the Combination of Direct and Inverse Photoemission. *Chem. Phys.* 2006, 325, 99–112.

64. Hill, I. G.; Kahn, A.; Soos, Z. G.; Pascal, J. R. A. Charge-Separation Energy in Films of π -Conjugated Organic Molecules. *Chem. Phys. Lett.* **2000**, *327*, 181–188.

TOC Graphic



Supporting Information: Hybrid Heterostructures to Generate Long-Lived and Mobile Photocarriers in Graphene

Pavel Valencia-Acuna,[†] Fatimah Rudayni,^{†,‡} Kushal Rijal,[†] Wai-Lun Chan,^{*,†} and Hui Zhao^{*,†}

†Department of Physics and Astronomy, The University of Kansas, Lawrence, Kansas 66045, United States

‡Department of Physics, Jazan University, Jazan 45142, Saudi Arabia

E-mail: wlchan@ku.edu; huizhao@ku.edu

Additional Carrier Dynamics

Figure 1(a) of the main text only shows the dynamics of the electrons and holes that are excited in the F₈ZnPc layer for clarify. In the experiments with a 3.18-eV pump, carriers are also excited in the MoS_2 and graphene layers, as shown in the left panel of Figure S1. As discussed in the main text, the electrons excited in F_8 ZnPc transfer to MoS₂. These electrons, along with those excited in MoS₂, are expected to transfer to graphene, driven by the conduction band offset between MoS₂ and graphene. The holes excited in MoS₂ could transfer to F₈ZnPc or graphene, since it has the lowest VBM. Meanwhile, the electrons and holes excited in graphene can undergo energy relaxation towards the band edge states by releasing their excess energy (dotted arrows). These processes all occur on ultrafast time scales. Hence, after about 1 ps, there are hole population in F₈ZnPc and imbalanced electron/hole population in graphene, as shown in the middle panel of Figure S1. Next, electron-hole recombination in graphene occurs on a few-ps time scale, resulting in layerseparated electron-hole population as shown in the right panel of Figure S1. For the WS₂based heterostructures, the additional carriers excited in WS₂ and graphene undergo similar ultrafast transients, as summarized in Figure S2. The end result after a few ps is also the layer-separated electron and hole populations.

In summary, the carriers excited in TMD and graphene layers do not alter the layer-

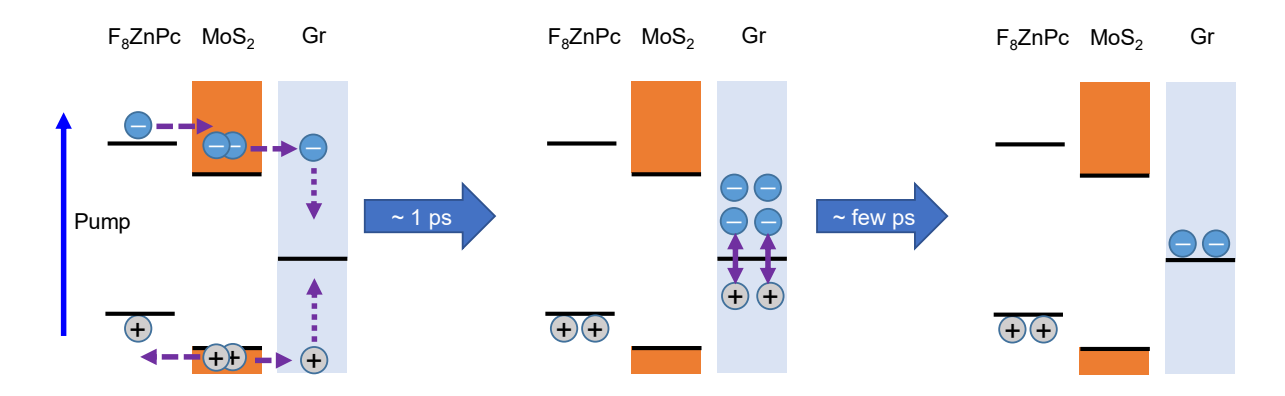


Figure S1: Time sequence of expected carrier dynamics immediately following pump pulse excitation of 3.18 eV in $F_8ZnPc/MoS_2/graphene$ heterostructure.

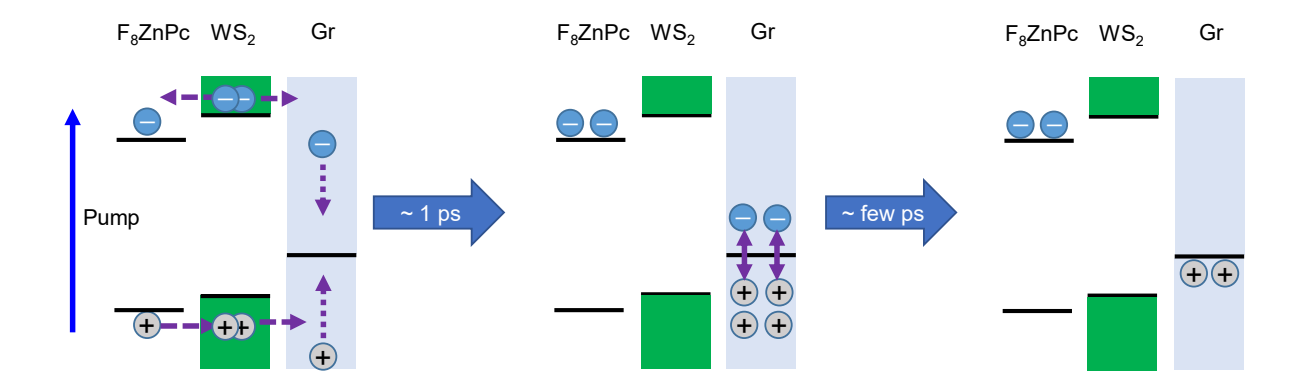


Figure S2: Time sequence of expected carrier dynamics immediately following pump pulse excitation of 3.18 eV in $F_8\text{ZnPc/WS}_2/\text{graphene}$ heterostructure.

separated electron-hole population after the short transient processes. Hence, these processed do not influence our discussion on the carrier diffusion in graphene, and are thus omitted in the main text.

Control Samples

For comparison, two control samples are fabricated and measured along with the heterostructure samples discussed in the main text.

First, differential reflectance of a monolayer graphene sample is shown in Figure S3. Here, a 1.57-eV pump pulse injects photocarriers, which dynamics is monitored by a 0.83-eV probe. The signal decays exponentially, with a time constant of 1.8 ± 0.2 ps. This results is consistent with previously established short lifetime of photocarriers in graphene. $^{1-4}$

Second, a heterostructure sample of $F_8ZnPc/graphene$ is studied to demonstrate the effect of the middle TMD layers. This sample is obtained on the same substrate of the trilayer heterostructure samples. Since F_8ZnPc is uniformly deposited on graphene, regions of graphene that are not covered by TMD can be naturally used as such a control sample. Figure S4 shows the measured differential reflectance signal. A 3.18-eV and 5- μ J cm⁻² pump pulse excites both layers. A 1.59-eV probe monitors carrier population in the graphene layer, which has a lifetime of about 1.6 \pm 0.4 ps (red curve). This experiment shows that, without

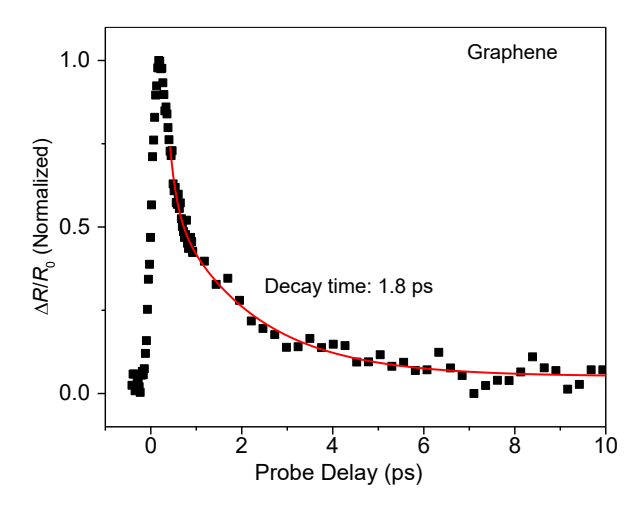


Figure S3: Differential reflectance of monolayer graphene measured with a 1.57-eV and 1.5- μ J cm⁻² pump and a 0.83-eV probe. The sample is at room temperature.

the middle layer, both electrons and holes excited in F_8 ZnPc can transfer to graphene and recombine rapidly. Hence, the insertion of the TMD middle layer is essential for separating the electrons and holes to extend their lifetime in graphene.

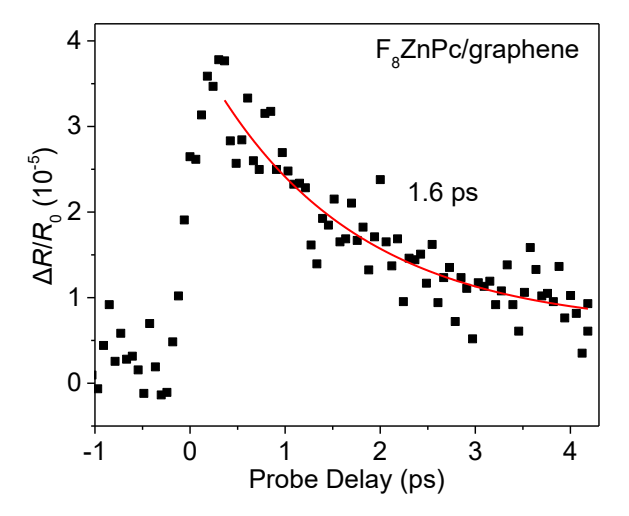


Figure S4: Differential reflectance of a heterostructure formed by F_8ZnPc and graphene measured with a 3.18-eV and 5- μJ cm⁻² pump and a 1.59-eV probe. The sample is at room temperature.

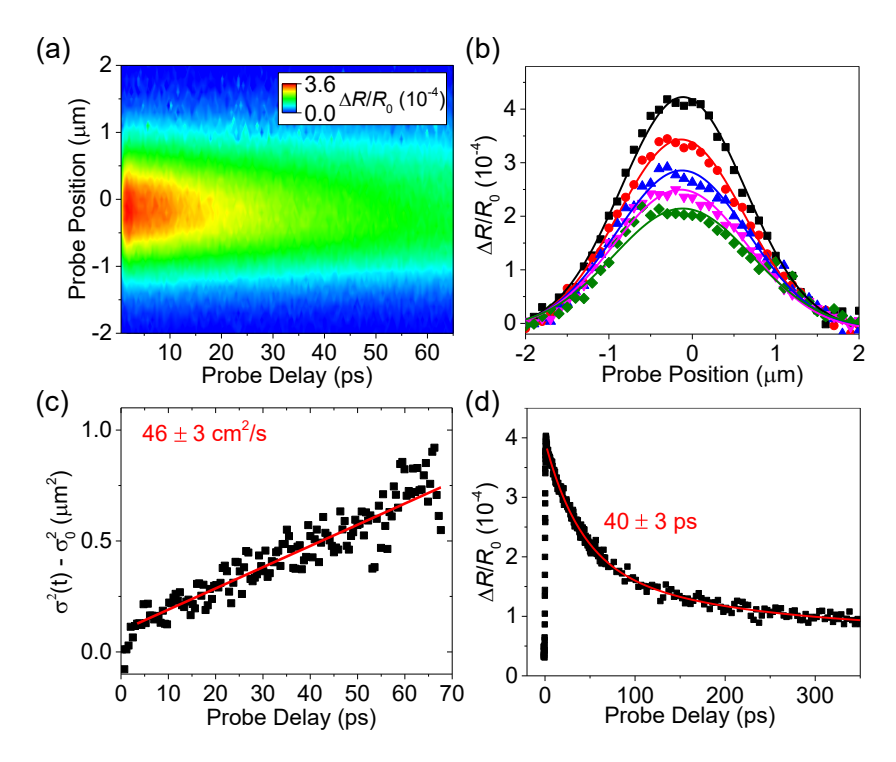


Figure S5: Photocarrier dynamics in a $F_8ZnPc/7L-WS_2/graphene$ heterostructure sample. (a)Spatiotemporally resolved differential reflectance. (b) Selected spatial profiles of differential reflectance. The probe delays are 5.5 (black), 20.4 (red), 35.3 (blue), 50.2 (pink), and 65.0 ps (green). The solid curves are Gaussian fits. (c) Change of the variance of the spatial distribution as a function of probe delay. The red line is a linear fit that gives a diffusion coefficient of 46 cm 2 s $^{-1}$. (d) Peak differential reflectance as function of probe delay, measured with the pump and probe spots overlapped. The red curve is an exponential fit with a decay time constant of 40 ps.

Heterostructure Sample with a Thick Middle Layer

To confirm the trend of increasing the carrier diffusion coefficient in graphene with thicker TMD middle layers, an additional heterostructure sample, $F_8ZnPc/7L-WS_2/graphene$, is studied. The 7L WS₂ is expected to have a bandstructure similar to bulk WS₂, while providing even larger charge separation and dielectric screening than the 4L WS₂. Transient absorption measurements are performed on this sample, with the same experimental conditions are the other WS₂-based heterostructures. Figure S5 summarizes the spatiotemporally resolved differential reflectance signal with 3.18-eV and 1.4 μ J cm⁻² pump and 1.59-eV probe pulses. By fitting the spatial profiles at different probe delays with Gaussian function [with a few examples shown in Figure S5(b)], the change of the variance is obtained and plotted in

Figure S5(c). The linear fit shown as the red line in Figure S5(c) yields a diffusion coefficient of $46 \pm 3 \text{ cm}^2 \text{ s}^{-1}$. Finally, the peak signal is plotted in Figure S5(d) as a function of probe delay. An exponential fit gives a decay time constant of $40 \pm 3 \text{ ps}$.

Photocarrier Lifetime in TMD/Graphene Bilayer Heterostructures

Table 1: Previously reported photocarrier lifetimes in TMD/graphene bilayer heterostructures. The reference numbers are those in the main text.

Heterostructure	Lifetime	Citation	Ref. #
$\mathrm{MoS}_{2}/\mathrm{Gr}$	1 ps	Lane et. al. Nano Futures 2, 035003 (2018)	[19]
$\mathrm{MoS}_{2}/\mathrm{Gr}$	2 ps	Tran et. al. ACS Nano 14, 13905 (2020)	[20]
MoS_2/Gr	1 ps	Luo et. al. Nano Lett. 21, 8051 (2021)	[21]
$\overline{\mathrm{WS}_2/\mathrm{Gr}}$	3.5 ps	He et. al. Nat. Commun. 5, 5622 (2014)	[22]
WS_2/Gr	1 ps	Yuan et. al. Sci. Adv. 4, e1700324 (2018)	[23]
$\overline{\mathrm{WS}_2/\mathrm{Gr}}$	1 ps	Aeschlimann et. al. Sci. Adv. 6, eaay0761 (2020)	[24]
$-WS_2/Gr$	4 ps	Ferrante et. al. PNAS 119, e2119726119 (2022)	[25]
$\overline{\mathrm{WSe}_2/\mathrm{Gr}}$	2.4 ps	Tan et. al. ACS Photo. 4, 1531 (2017)	[26]
WSe_2/Gr	2.3 ps	Zhou et. al. Sci. Adv. 7, eabg2999 (2021)	[27]

References

- Huang, L.; Hartland, G. V.; Chu, L. Q.; Luxmi,; Feenstra, R. M.; Lian, C.; Tahy, K.; Xing, H. Ultrafast transient absorption microscopy studies of carrier dynamics in epitaxial graphene. *Nano Lett.* 2010, 10, 1308.
- George, P. A.; Strait, J.; Dawlaty, J.; Shivaraman, S.; Chandrashekhar, M.; Rana, F.;
 Spencer, M. G. Ultrafast optical-pump terahertz-probe spectroscopy of the carrier relaxation and recombination dynamics in epitaxial graphene. Nano Lett. 2008, 8, 4248.
- Breusing, M.; Kuehn, S.; Winzer, T.; Malicacute, E.; Milde, F.; Severin, N.; Rabe, J. P.; Ropers, C.; Knorr, A.; Elsaesser, T. Ultrafast nonequilibrium carrier dynamics in a single graphene layer. *Phys. Rev. B* 2011, 83, 153410.

4. Ruzicka, B. A.; Wang, S.; Werake, L. K.; Weintrub, B.; Loh, K. P.; Zhao, H. Hot carrier diffusion in graphene. *Phys. Rev. B* **2010**, *82*, 195414.